⌘ *Author's Choice*

THE JOURNAL OF BIOLOGICAL CHEMISTRY VOL. 284, NO. 33, pp. 22310–22321, August 14, 2009

Three-dimensional Structure of $Ca_V3.1$

COMPARISON WITH THE CARDIAC L-TYPE VOLTAGE-GATED CALCIUM CHANNEL MONOMER ARCHITECTURE[*] [◆]

Received for publication, May 5, 2009, and in revised form, June 8, 2009 Published, JBC Papers in Press, June 11, 2009, DOI 10.1074/jbc.M109.017152

Conor P. Walsh[‡1], **Anthony Davies**[§2], **Adrian J. Butcher**[§], **Annette C. Dolphin**[§2], **and Ashraf Kitmitto**[‡3]

From [‡]*Cardiovascular Medicine, School of Clinical and Laboratory Sciences, Faculty of Medical and Human Sciences, University of Manchester, Manchester M13 9NT and the* [§]*Department of Neuroscience, Physiology and Pharmacology, University College London, Gower Street, London WC1E 6BT, United Kingdom*

Calcium entry through voltage-gated calcium channels has widespread cellular effects upon a host of physiological processes including neuronal excitability, muscle excitation-contraction coupling, and secretion. Using single particle analysis methods, we have determined the first three-dimensional structure, at 23 Å resolution, for a member of the low voltage-activated voltage-gated calcium channel family, $Ca_V3.1$, a T-type channel. $Ca_V3.1$ has dimensions of ~115 × 85 × 95 Å, composed of two distinct segments. The cytoplasmic densities form a vestibule below the transmembrane domain with the C terminus, unambiguously identified by the presence of a His tag being ~65 Å long and curling around the base of the structure. The cytoplasmic assembly has a large exposed surface area that may serve as a signaling hub with the C terminus acting as a "fishing rod" to bind regulatory proteins. We have also determined a three-dimensional structure, at a resolution of 25 Å, for the monomeric form of the cardiac L-type voltage-gated calcium (high voltage-activated) channel with accessory proteins β and $\alpha_2\delta$ bound to the ion channel polypeptide $Ca_V1.2$. Comparison with the skeletal muscle isoform finds a good match particularly with respect to the conformation, size, and shape of the domain identified as that formed by α_2. Furthermore, modeling of the $Ca_V3.1$ structure (analogous to $Ca_V1.2$ at these resolutions) into the heteromeric L-type voltage-gated calcium channel complex volume reveals multiple interaction sites for β-$Ca_V1.2$ binding and for the first time identifies the size and organization of the $\alpha_2\delta$ polypeptides.

To date, five different types of voltage-gated calcium channels (VGCCs)[4] have been identified, L, N, P/Q, R, and T, and classified according to their physiological and pharmacological characteristics (1–3). On the basis of their electrophysiological properties, VGCCs can be divided into two classes: high voltage-activated (HVA) and low voltage-activated (LVA). T-type Ca^{2+} channels form the LVA family and are characterized by their low threshold of activation, small single channel conductance, slow deactivation, and a low sensitivity to classical blockers of HVA channels (4–6). T-type channels have a central role regulating, for example, cardiac pacemaking of sinoatrial node cells and tonic firing patterns in neurons (5). Three T-type channel isoforms have been identified and cloned: $Ca_V3.1$, $Ca_V3.2$, and $Ca_V3.3$, with each isoform possessing several splice variants showing distinct functional properties (reviewed in Ref. 7).

Each VGCC is composed of a pore-forming polypeptide termed the Ca_V $\alpha1$-subunit, with 10 mammalian $\alpha1$ isoforms identified, divided into three subfamilies: Ca_V1–3 (8). Housed within the Ca_V $\alpha1$ subunit are the calcium pore, voltage-sensing apparatus, drug binding sites, and numerous structural determinants required for binding auxiliary subunits and other regulatory proteins. Analysis of the amino acid sequences and predicted secondary structure of the T-type channels suggests a similar topology to the HVA Ca_V α_1 subunits and K^+ and Na^+ channels, implying that they are evolutionarily related (5).

HVA channels are heteromeric complexes formed by the Ca_V $\alpha1$ polypeptide, with several accessory subunits non-covalently bound. For example, the cardiac L-type voltage-gated calcium channel is formed by the $Ca_V1.2$ subunit in association with the soluble β-polypeptide localized to the intracellular side of the plasma membrane and a largely extracellular $\alpha_2\delta$ subunit (9, 10). The β-subunit has a role in regulating activation, inactivation, and voltage dependence as well as targeting of $Ca_V1.2$ to the plasma membrane. The crystal structure of the core region of the β-polypeptide in complex with a peptide corresponding to the interacting region of the $Ca_V1.2$ (AID) has been described (11, 12), revealing that it is comprised of two domains, a type 3 Src homology (SH3) domain and a guanylate kinase-like domain. $Ca_V1.2$ is associated, on the extracellular side of the membrane, with the $\alpha_2\delta$ subunit, the product of post-translational cleavage of a single gene comprised of a glycosylated extracellular $\alpha2$ domain linked by disulfide bonds to the transmembrane δ polypeptide, which is also mainly extracellular and glycosylated. Four isoforms of $\alpha_2\delta$ have been identified (13, 14). The role of the $\alpha_2\delta$ protein is not as well understood as that of the β-subunit, but it has been shown to increase the current amplitude and have effects on inactivation (15). An

* This work was funded by a grant from the British Heart Foundation (BHF).
◆ This article was selected as a Paper of the Week.
⌘ *Author's Choice*—Final version full access.
[1] Recipient of BHF Ph.D. Studentship FS/05/018.
[2] Funded by the Medical Research Council.
[3] Recipient of BHF Award BS/97002. To whom correspondence should be addressed: Third Fl., Core Technology Facility, Cardiovascular Group, Grafton St., Manchester M13 9NT, UK. Tel.: 44-1613064186; Fax: 441612751183; E-mail: ashraf.kitmitto@manchester.ac.uk.
[4] The abbreviations used are: VGCC, voltage-gated calcium channels; LTCC, L-type voltage-gated calcium channel; LVA, low voltage-activated; HVA, high voltage-activated; DTT, dithiothreitol; CHAPS, 3-[(3-cholamidopropyl)-dimethylammonio]-1-propanesulfonic acid; Ni-NTA, nickel-nitrilotriacetic acid; FSC, Fourier shell correlation; TM, transmembrane; ConA, concanavalin A; AID, α-interaction domain.

additional membrane-spanning auxiliary subunit, γ, was initially thought to be unique to the skeletal muscle LTCC; however, recent studies have identified neuronal isoforms, although it remains unclear whether they have any role as calcium channel subunits (16, 17).

We report here the purification of a recombinant $Ca_V3.1$, leading to the calculation of the first three-dimensional structure for a member of the LVA channel family. $Ca_V3.1$ is formed by two distinct segments, which we have been able to assign to the transmembrane and cytoplasmic domains. We have identified the C-terminal domain that forms a tail that winds around the base of the structure, providing insights as to how this channel may be regulated through the binding of accessory/regulatory proteins and/or long range conformational movements. Furthermore, we have been able to utilize this new three-dimensional structure to probe the assembly of the polypeptides forming the cardiac LTCCs after having also calculated a novel three-dimensional structure for the monomeric form of the channel purified from bovine heart. At the resolutions described here, $Ca_V3.1$ can be considered analogous to $Ca_V1.2$; see Fig. 1*A* for a sequence alignment overview. No mandatory auxiliary subunits for the T-type, LVA, channels have been identified. However, studies have shown that co-expression of $Ca_V3.1$ with $\alpha_2\delta$ subunits led to a 2-fold increase in T-type-mediated currents (18), and thus this model may also provide an insight as to how accessory proteins may associate with $Ca_V3.1$ to exert regulatory effects.

EXPERIMENTAL PROCEDURES

$Ca_v3.1$ Expression and Purification—The $Ca_V3.1$ rat neuronal clone was a kind gift from Dr. Edward Perez-Reyes (19). The baculovirus vector pFastBac-HTa, the Bac-to-Bac baculovirus expression system, and the S*f*9 cells were purchased from Invitrogen. $Ca_V3.1$ containing a C-terminal c-Myc and decahistidine (His_{10}) tag (20) was subcloned into the baculovirus vector pFastBac-HTa. Recombinant baculoviruses were generated using the Bac-to-Bac system (Invitrogen). S*f*9 insect cells were cultured in TNM-FH medium (Sigma T3285) supplemented with 10% (v/v) fetal bovine serum and were split when confluent. For protein expression, S*f*9 cells, 70–80% confluent, were infected with recombinant baculoviruses at a multiplicity of infection of 1–2. They were then incubated at 27 °C for 72 h.

Virus-infected S*f*9 cells expressing the $Ca_V3.1$ were harvested 72 h after infection by centrifugation at 1000 × *g* for 5 min. The resulting cell pellets were resuspended in 10 ml of buffer containing 20 mM Tris, pH 8.0, 150 mM NaCl, and 1 mM DTT. All buffers also contained protease inhibitors in the form of Complete EDTA-free protease inhibitor mixture (Roche Applied Science), with one tablet dissolved for every 50 ml of buffer. Cells were lysed by sonication for 3 × 30 s. The mixture was then centrifuged at 1000 × *g* for 5 min to remove the large particulate matter. The resulting supernatant, containing the S*f*9 cell membranes, was then centrifuged at 50,000 × *g* for 1 h. The pellet was then resuspended in 10 ml of buffer containing 20 mM Tris, pH 8.0, 150 mM NaCl, 20 mM imidazole, 1 mM DTT, 1% (w/v) CHAPS, and protease inhibitors and incubated for 1 h on a rolling platform at 4 °C. The solubilized membrane protein then underwent centrifugation at 20,000 × *g* for 30 min at 4 °C to clear any unsolubilized material. The resulting supernatant was diluted 1:1 with buffer containing 20 mM Tris, pH 8.0, 150 mM NaCl, 20 mM imidazole, and 1 mM DTT and applied to a 1-ml Ni-NTA column (HIS-Select® nickel affinity gel (Sigma)), which had been pre-equilibrated with a buffer containing 20 mM Tris, pH 8.0, 150 mM NaCl, 20 mM imidazole, 1 mM DTT, 0.5% (w/v) CHAPS. The gel matrix was washed with 5 volumes of equilibration buffer: 20 mM Tris, pH 8.0, 150 mM NaCl, 20 mM imidazole, 1 mM DTT, 0.5% (w/v) CHAPS. The protein solution was then added to the matrix, and this was left for 1 h on a rolling platform at 4 °C. The column was then washed with 20 volumes of equilibration (wash) buffer, and finally, the bound protein was eluted by the addition of 1 column volume of equilibration buffer containing 350 mM imidazole. This final step was repeated four times, and thus four eluted fractions were collected. The eluted protein was concentrated using a Centricon YM-50, applied to a size exclusion column (Sephacryl S-200), and eluted off using the buffer above (without the imidazole and with 50 mM NaCl). $Ca_V3.1$-containing fractions were applied to a preswollen microgranular anion exchanger diethylaminoethyl (DEAE) cellulose (DE52, Whatman). $Ca_V3.1$ was eluted using a step NaCl gradient (25–500 mM, using 25 mM increments). SDS-PAGE and Western blotting (anti-$Ca_v3.1$, Santa Cruz Biotechnology sc-25690) were employed to determine the purity and characterize the purified protein at each step with protein eluting between 250 and 350 mM NaCl from the DEAE-column found to be pure $Ca_V3.1$ (see Fig. 1*A*).

Cardiac LTCC Purification—Sarcolemmal membranes were prepared from bovine heart according to Ref. 21. All buffers throughout the purification were supplemented with a protease inhibitor mixture containing 0.1 mM phenylmethylsulfonyl fluoride, 1 mM benzamidine, 1 μM pepstatin A, and 1 μM L-trans-epoxysuccinyl-leucylamide-(-4-guananido)-butane (E64). As described previously (22), LTCCs were solubilized from the sarcolemmal membranes (protein concentration of 2 mg/ml) by incubation with 1% (w/v) digitonin (detergent:protein 5:1), in 20 mM Tris, pH 7.5, 2 mM $CaCl_2$, for 45 min with gentle agitation at 4 °C. The solubilized protein was then loaded onto a DEAE-column (20 ml) equilibrated with the solubilization buffer. Unbound protein was removed by washing with 1.5 column volumes of 0.1% (w/v) digitonin in 20 mM Tris, pH 7.5, followed by a second wash with 1% (w/v) decyl-β-D-maltoside substituted for the digitonin. Protein was then eluted from the column with a linear NaCl gradient (0–0.5 M) in 1% w/v decyl-β-D-maltoside, 20 mM Tris, pH 7.5, 2 mM $CaCl_2$. The LTCC-containing fractions were then concentrated using a Centricon YM-50 and applied to a size-exclusion column (Sephacryl S-300). The channel-containing fractions were then applied to a wheat germ agglutinin (WGA)-column, and the purification procedure followed that described in Ref. 22. Purified cardiac LTCC preparations were examined by SDS-PAGE, and native gels were as described in Ref. 23. Protein bands from gels were transferred to nitrocellulose using a Bio-Rad Transblot apparatus. Monoclonal antibodies against the cardiac LTCC α_2 subunits were purchased from Abcam, and antisera and affinity-purified antibodies raised against a β-subunit peptide (Ab2491) were prepared as described previously (23, 24).

Electron Microscopy and Image Analysis—Samples were examined using standard negative staining techniques with 2% (w/v) uranyl acetate. Images of the LTCC complex and $Ca_V3.1$ were recorded between a 0.55–0.96 μm and 0.65–1.05 μm defocus range, respectively, on a Tecnai 12 transmission electron microscope operated at 100 kV, at a calibrated magnification of ×47,800. Micrographs were scanned using an IMACON scanner at 3.6 Å/pixel at the specimen level. $Ca_V3.1$ and cardiac LTCC samples were checked for homogeneity and presentation of different views. Matrix analysis of sampling over Euler angles, ϕ, θ, and ψ, showed a good coverage of three-dimensional space for each data set (not shown). The contrast transfer function (CTF) was determined for each image using CTFIT (part of the EMAN software). As discussed by Adair *et al.* (25), images were corrected for phase effects only. The resolution of the final three-dimensional volumes for $Ca_v3.1$ and the cardiac LTCC were assessed following established procedures (26). In brief, each data set was divided into two, with volumes calculated for the two subsets, and the resolution was estimated by the Fourier shell correlation (FSC) coefficient with the resolution limit taken to be where the FSC value fell below 0.5. All models were generated using the UCSF Chimera program.

Three-dimensional Reconstruction of Recombinant $Ca_v3.1$—The three-dimensional structure of the recombinant $Ca_V3.1$ was generated using the common line projection matching methods employed in EMAN (27) with no symmetry applied (C1). Three-dimensional reconstructions of small asymmetric proteins are complex, and rigorous experimentation must be undertaken to ensure that the features in the final model are robust. A wide variety of starting models were tested including Gaussian blobs, transmembrane domain of $K_V1.2$ (PDB entry 2R9R, edited), and the full $K_V1.2$ crystal structure (2R9R) filtered to an appropriate resolution. In all reconstructions the principal structural features were consistent, indicating the fidelity of the final three-dimensional reconstruction. Approximately 11,500 particles were selected interactively using the graphical interface boxer (EMAN image processing software) into a box of 64 × 64 pixels (230 × 230 Å). Particles were band-pass-filtered and centered, and a preliminary three-dimensional model was calculated from a set of unbiased reference-free class averages showing different orientations of the complex (using the refine2d.py program under EMAN). The three-dimensional model was iteratively refined at each step using a projection matching routine, whereby projections with uniformly distributed orientations of the preliminary three-dimensional model were used as references for classification of the raw data set, with the class averages from this step used to construct a new three-dimensional model. Refinement was carried out with an angular coverage of 7° generating 388 classes containing between 10 and 48 particles per class. The final reconstruction included 86% of the selected images. Convergence, *i.e.* stabilization of the three-dimensional structure, was monitored by examining the FSC of the three-dimensional models generated from each iteration.

The presence of the C-terminal His tag allowed labeling of the $Ca_V3.1$ C terminus using Ni-NTA-gold® (Nanoprobes Inc). Excess Ni-NTA-gold was added to the purified $Ca_V3.1$ and incubated for 3 h. Aliquots were then stained with uranyl acetate as above. Approximately 4,500 $Ca_V3.1$ particles with a gold label associated were selected. The class averages shown in Fig. 3 illustrate that a good sampling of different orientations of labeled $Ca_V3.1$ was observed. The same initial start model employed for the three-dimensional reconstruction of the unlabeled $Ca_V3.1$ was used for the gold-labeled channel.

Three-dimensional Reconstruction of Purified Cardiac LTCCs—The three-dimensional structure of the cardiac LTCC was generated using the same methodology as described above, determined with no symmetry imposed, *i.e.* C1. Approximately 4,300 particles were selected interactively using the graphical interface boxer (EMAN image processing software) into a box of 88 × 88 pixels (316 × 316 Å). Particles were band-pass-filtered and centered, and a preliminary three-dimensional model was calculated from a set of unbiased reference-free class averages showing different orientations of the complex. The three-dimensional model was iteratively refined at each step using a projection matching routine, carried out with an angular coverage of 10 degrees generating 179 classes with between 7 and 42 images per class. The final reconstruction included 87% of the selected images. As described above, to ensure that the features of the resulting C1 volume were consistent, several different start models from class averages derived from startnr-classes and refine2d.py, as well as using a sphere (makeinitialmodel.py), were employed. Fourier shell correlation between each model was used to determine convergence to the final model. A low pass Gaussian filter to 25 Å was applied to the final three-dimensional volume in accordance with the resolution assessment.

Cardiac LTCC Labeling—Concanavalin A (Sigma) (stock 5 mg/ml in 10 mM Hepes, 50 mM NaCl, 1 mM $CaSO_4$, 1 mM $MnCl_2$, pH 7) was added in a 3-fold excess to the purified cardiac LTCC (following the method described in Ref. 28) for 30 min on ice. Samples were then examined by transmission electron microscope after staining with 2% (w/v) uranyl acetate. Micrographs were scanned as above, and LTCC-Con A conjugates were selected (box size 104 × 104 pixels; 374 × 374 Å), aligned, and classified using standard programs in the SPIDER software package (29).

RESULTS

$Ca_V3.1$ was expressed and purified from S*f*9 cells. $Ca_V3.1$ is a small (~250-kDa, rat) asymmetric protein composed of 24 putative transmembrane segments, grouped into four domains, which are connected by intracellular loops, with a large (~46 kDa) cytoplasmic C-terminal domain. We have previously characterized this expressed protein and shown it to be functional (20). Serial chromatographic techniques were employed, including nickel affinity gel, to exploit the presence of the polyhistidine tag. Size exclusion and ion exchange steps were also introduced to further purify the sample, leading to a single band on a SDS-PAGE at ~250 kDa, corresponding to the predicted molecular mass of $Ca_V3.1$ (Fig. 1*B*, *lane 1*). The identity of the purified protein as $Ca_V3.1$ was confirmed by Western blotting methods (Fig. 1*B*, *lane 2*, anti-$Ca_V3.1$; *lane 3*, anti-His). Approximately 50 μg of highly purified $Ca_V3.1$ protein was isolated from 49 mg of S*f*9 cells after sonication.

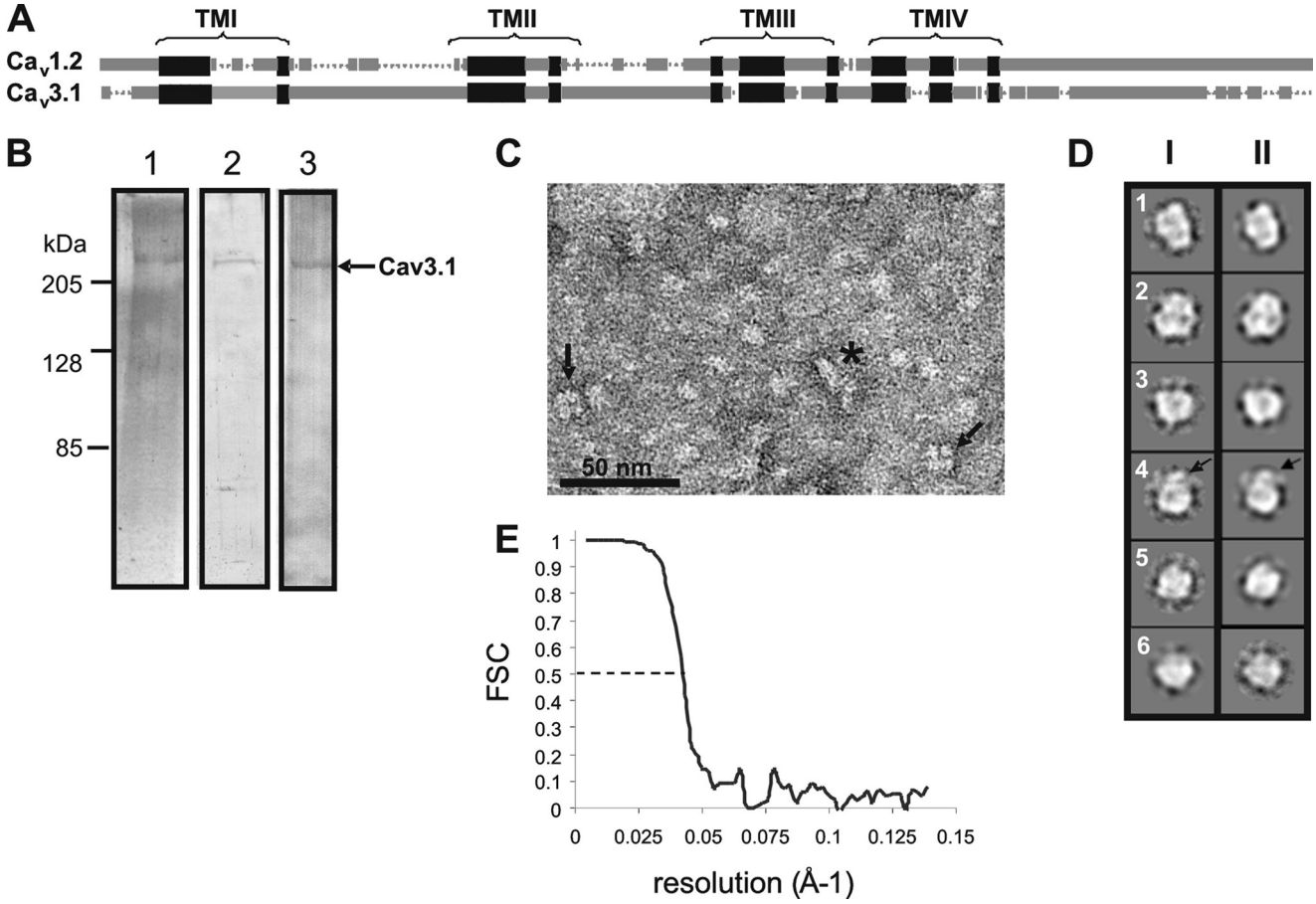

FIGURE 1. **Characterization, purification and image analysis of the T-type voltage gated calcium channel $Ca_v3.1$.** *A*, schematic overview of a sequence comparison of voltage-gated calcium Ca^{2+} channel subunits $Ca_V1.2$ and $Ca_V3.1$. Sequence alignment was carried out using ClustalW (37). *Solid regions* indicate aligned sequences (*black blocks* correspond to the transmembrane helices); extracellular loops comprising <10 amino acids are not depicted. *B, lane 1*, silver-stained 10% SDS-PAGE of purified recombinant $Ca_V3.1$ revealing a single polypeptide band at ~250 kDa. *Lane 2*, identification of the purified $Ca_V3.1$ by Western blotting (anti-$Ca_V3.1$, Santa Cruz Biotechnology sc-25690). *Lane 3*, Western blot of the purified $Ca_v3.1$ using an anti-His (Santa Cruz Biotechnology) antibody revealing a single protein product (recombinant $Ca_v3.1$ with a C-terminal His tag) at ~250 kDa. *C*, field of negatively stained (2% w/v uranyl acetate) recombinant $Ca_V3.1$ showing white protein particles presenting a range of orientations ~85–115 Å in size. The *asterisk* indicates a small area of aggregation that is easily distinguishable from the single $Ca_V3.1$ complexes. The *black arrows* indicate square-shaped particles with a side length of ~100 Å. *D*, *column I*, examples of reference-free class averages obtained by alignment of the raw data that are representative of the range of multiple orientations sampled (box size 230 × 230 Å). *Column II*, corresponding back projections of the final three-dimensional volume illustrate that the structural features are consistent with those shown in the class averages. *E*, Fourier shell correlation plot indicating at a correlation of 0.5 that the three-dimensional $Ca_V3.1$ structure is at a resolution of 23 Å.

Structure of $Ca_v3.1$ at 23 Å—Single particle analysis has proven particularly suitable for structural studies of large macromolecular complexes such as the ribosome (for review, see Ref. 30) and proteins with complex symmetry *e.g.* viruses (31); however, there are also a number of reports for successful reconstructions of relatively small asymmetric proteins (*e.g.* Refs. 25, 32–34). Examination of micrographs of purified $Ca_V3.1$ found a homogeneous population of particles, presenting multiple views of the channel. Encouragingly, square-shaped particles with a side length of ~100 Å were occasionally observed (indicated on Fig. 1*C*) that may represent a view of the channel perpendicular to the membrane plane in keeping with the putative pseudo four-fold symmetry of the transmembrane domains. The Fourier common lines projection-matching method was employed using the EMAN software package (27) to calculate a three-dimensional structure. In total, 11,500 $Ca_V3.1$ particles, ranging in size from ~80 to 120 Å, were selected. Fig. 1*D* presents examples of class averages and corresponding reprojections of the final three-dimensional volume, illustrating that the structure is consistent with the class averages. *Image 1* shows a structure that is ~115 Å in length, narrowing to one end and ~85 Å at the widest point. The image below is slightly shorter and wider with two distinct domains resolved. The complexes in rows 3 and 4 are almost square-shaped, ~85 × 95 Å, and are characterized by a central region of low density (*i.e.* averages appear slightly darker in the middle). The *arrow* on *image 4* highlights a small density we have termed the tail that protrudes from the body of the complex. Although *image 5* is similar in shape and size to that presented in *row 3*, it does not display a mid region of low density and thus likely represents a different view of the complex. *Image 6* shows a class average that is consistent with the observation of tetragonal particles with side lengths of ~100 Å. The Fourier shell correlation plot shown in Fig. 1*E* indicates that the resolution of the final three-dimensional volume is ~23 Å at a correlation of 0.5.

The three-dimensional reconstruction of purified $Ca_V3.1$ (Fig. 2) yielded a complex ~115 Å tall with a width and depth of

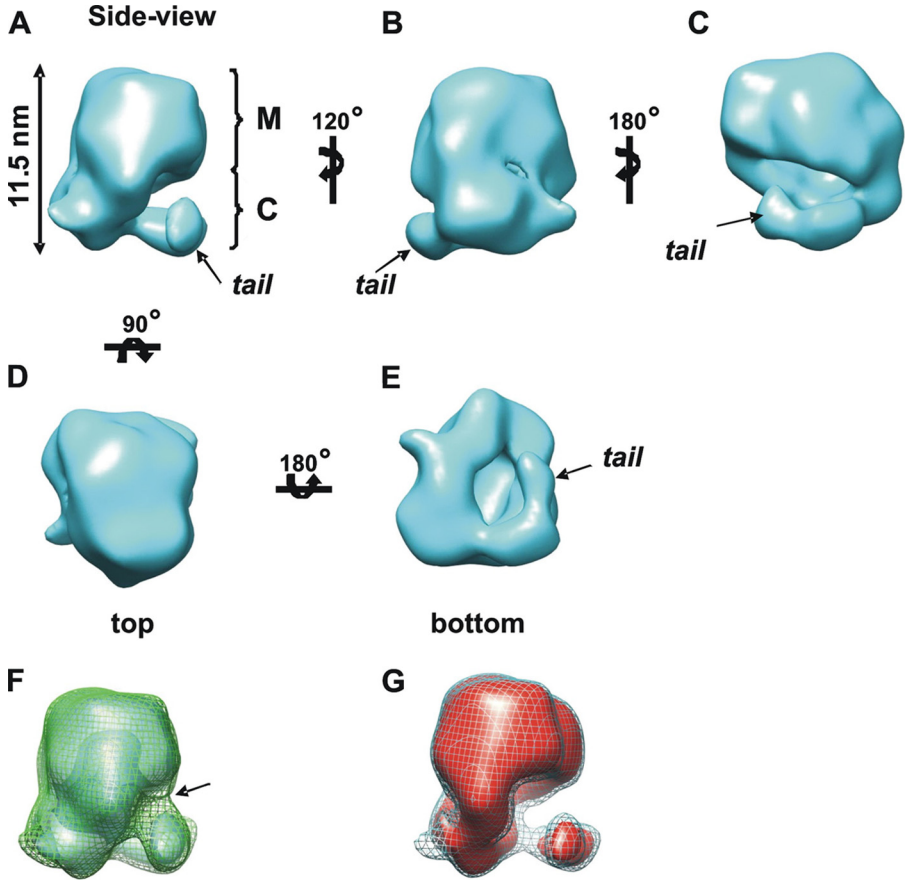

FIGURE 2. **Three-dimensional structure of $Ca_v3.1$ at 23 Å.** *A*, putative side view of $Ca_V3.1$, displayed for a protein mass of ~320 kDa, revealing a structure ~115 Å tall and ~85–95 Å across. The complex is formed by two domains we have termed *M* and *C*, as illustrated on the figure. *B* and *C*, rotation of this view around the *y* axis reveals further details with *C* showing that the density we have called the tail is ~65 Å in length, extends out, and curls around the base of the structure. *D*, a view of the upper surface of domain M revealing it to be relatively flat, ~85 × 95 Å in size. *E*, rotation of the view in *D* 180° around the *x* axis to show the base of the structure. *F*, three-dimensional structure of $Ca_V3.1$ displayed at two volume thresholds; *turquoise solid surface* corresponds to a protein mass of ~320 kDa, and *green mesh* corresponds to a protein mass of ~620 kDa. *G*, three-dimensional structure of $Ca_V3.1$ displayed at two volume thresholds; the *red solid surface* (~230 kDa) and *turquoise mesh* (~320 kDa) show that the principal structural features are consistent between maps, although at higher thresholds, the tail is separated from the other cytoplasmic protein domains by a small gap indicated by the *arrow* in *F*.

~85 × 95 Å. A putative side view of $Ca_V3.1$ is presented in Fig. 2*A*. It is comprised of two distinct sections: an upper compact domain labeled *M* ~50–60 Å in height and 85 × 95 Å across as viewed from the top (Fig. 2, *A* and *D*) and a lower portion labeled *C* formed from a number of densities (Fig. 2, *B* and *C*). Fig. 2*E* shows that the structure of $Ca_V3.1$ is open from the bottom and reveals that the domain we identified as the tail in class average 4 (Fig. 1*D*) is ~65 Å long and curls around the base to form a horseshoe shape. The three-dimensional structure of $Ca_V3.1$ is displayed to encapsulate a protein mass of ~320 kDa (including detergent micelle and residual lipid). It is estimated that the amount of detergent associated with purified intrinsic membrane proteins increases the mass of the protein, depending on the detergent, by a factor of 0.3–1.5 (35). Therefore, the structure is also presented (Fig. 2, *F* and *G*) at two other volume thresholds. It can be seen (Fig. 2*F*) that there are few differences between the structural features, except that at the lower threshold, the tip of the tail forms a contact with the lower portion of domain M, as indicated by the *arrow*. At a higher threshold (corresponding to a protein mass of ~230 kDa, Fig. 2*G* displayed in *red surface render*), the global features and characteristics identified in *panels A–F* remain consistent.

Orientation of $Ca_v3.1$—Using Ni-NTA-gold (Nanoprobes Inc.), we have labeled the polyhistidine tag at the C terminus of $Ca_V3.1$ to identify its position within the three-dimensional structure. The Ni-NTA-gold conjugate is visualized as an electron-dense black globular domain ~1.8 nm in diameter, under the conditions employed here, and has the advantage of being able to bind closely to the His tag because there are no additional proteins attached. We calculated a new three-dimensional structure from 4,500 $Ca_V3.1$ particles with a gold label bound, using the same starting model and refinement parameters as those used for determining the unlabeled structure in Fig. 2. The principal structural features of the labeled $Ca_V3.1$ matched well to those of the unlabeled structure illustrated by the close similarity between some examples of class averages from both data sets shown in Fig. 3*A*. The two volumes were superimposed, with the labeled structure displayed using negative thresholds to visualize the electron-dense gold conjugate. Different views of $Ca_V3.1$ are shown in Fig. 3, *B–E*, revealing the gold to be nestled between the tail and body of the complex and bound to the lateral portion of the tail. Thus we propose that this domain corresponds to the C terminus of $Ca_V3.1$. Moreover, the approximate volume encompassed by the tail domain, at thresholds displayed here, corresponds to a mass of ~50 kDa (based upon an average protein density of 1.22 g cm^{-3} or 0.735 Da/$Å^3$ (36)), which is in keeping with the predicted mass of ~46 kDa (amino acids 1823–2254) of the cytoplasmic C-terminal domain extending from transmembrane (TM) IVS6.

Fitting of the Crystal Structure of $K_v1.2$ to the Transmembrane Domain of $Ca_v3.1$—The transmembrane domain of $K_V1.2$ (PDB entry 2A79), equivalent in terms of size and predicted organization to the TM regions of $Ca_V3.1$, can be fitted into domain M (Fig. 3, *F–I*). Fig. 3*F* shows the top view of $Ca_V3.1$, and although a central pore is not resolved in the outer surface of the complex, a section taken through domain M (in the position indicated in Fig. 3*I* by the *dashed line*) reveals that the interior is formed by 3–4 domains organized in such a way that there is a central area of low density (Fig. 3*J*), which is consistent with the predicted topology of the TM domain. It should be noted that the definition of the

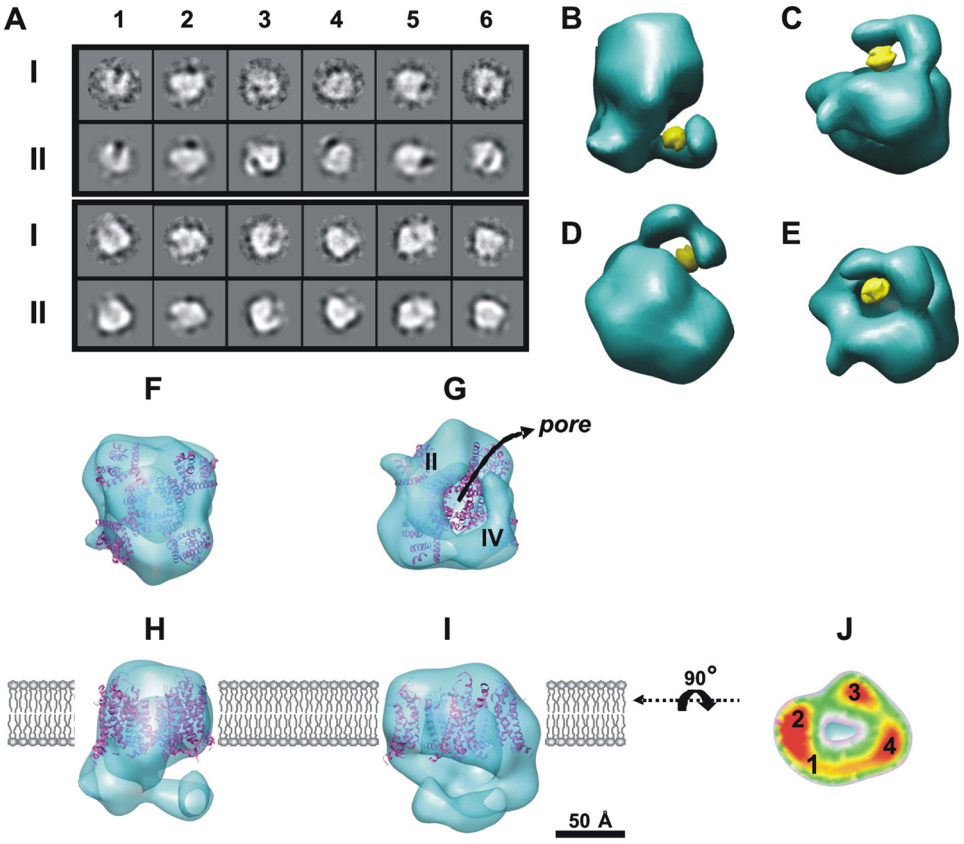

FIGURE 3. **Labeling of the C terminus of $Ca_v3.1$ and assignment of the transmembrane and cytoplasmic assemblies.** *A*, Ni-NTA-gold was incubated with purified recombinant $Ca_V3.1$ to identify the position of the polyhistidine-tagged C terminus. The *top panels* show a sample of some class averages (*row I*) and corresponding reprojections (*row II*) of the final three-dimensional volume of Ni-NTA-gold-labeled $Ca_V3.1$. The Ni-NTA-bound conjugate is electron-dense, and the gold particle is visualized as a *black domain* ~2 nm in diameter associated with the *white protein density*. The *bottom panels* show very similar class averages from the unlabeled $Ca_V3.1$ data set (*row I* with back projections presented below in *row II*). Images in *column 1* show a view that likely corresponds to the cytoplasmic side with the gold bound between two densities separated by a cavity and at one end. *Column 3* shows the gold to be nestled between the body of the complex and the tail comparable with the view shown in *panel C*. *Column 5* shows an elongated (side view ~115 Å long axis) with the gold toward one end (the class averages from the labeled and unlabeled data set are not aligned with respect to each other). Images in columns *2*, *4*, and *6* show views of the complex that are similar to the orientations presented in *panels C*, *D*, and *E*. Box size = 230 × 230 Å. *B–E* show the three-dimensional volume of the unlabeled $Ca_V3.1$ with the structure of $Ca_V3.1$ labeled with Ni-NTA-gold superimposed, with the main structural features matched and the labeled map displayed at negative thresholds (*gold density*) to display the position of the Ni-NTA-gold with respect to the protein structure. *F–J* illustrate the matching of the crystal structure of the potassium channel $K_V1.2$ (TM domain) to the three-dimensional structure of $Ca_V3.1$. *F*, putative top view of the complex showing that the crystal structure of $K_V1.2$ (PDB entry 2A79), *purple ribbon*, is accommodated within domain M. *G*, base of the complex viewed perpendicular to the membrane, revealing that the pore of $K_V1.2$ is open to the intracellular milieu through a passageway formed by domain C. The views shown in *H* and *I* illustrate that the TM domain of $K_V1.2$ is also compatible with the height of domain M, and thus the putative position of the lipid bilayer is proposed. *J*, a slice taken through the top of domain M as orientated in *panel I* at the position indicated by the *dashed line*. The section reveals between 3 and 4 protein densities arranged at the corners of the roughly square-shaped slice surrounding a region of low density. *Red*, *yellow*, *green*, *pink*, and *blue* correspond to thresholds at 6, 5, 4, 3 and 2 σ above the mean density.

interior of a protein structure applying negative staining techniques relies on the ability of the stain to penetrate the volume and is also influenced by the hydrophilic nature of the internal environment, and as such, caution should be taken when interpreting internal features. As would be expected, there is not an exact fit between the two as not only are we comparing a calcium channel with a potassium channel, but there will also be conformational effects upon the TM helices due to the presence of the cytoplasmic assembly in $Ca_V3.1$. However, this comparison serves to illustrate that the TM domain of $K_V1.2$ is accommodated within the section of $Ca_V3.1$ we have labeled M and fits in terms of both shape and overall size.

Fitting of $Ca_v3.1$ with the Three-dimensional Structure of the Cardiac L-type Voltage-gated Calcium Channel—A schematic representation of a sequence alignment of $Ca_V1.2$ and $Ca_V3.1$ is shown in Fig. 1*A*. There is an overall sequence identity of 19% between the two HVA and LVA channels (ClustalW (37)), although analysis of the individual domains finds a much higher match between the four repeat TM segments (I–IV). Using ClustalW, the average alignment between each TM segment is ~40%, with the T-Coffee scoring system (available from the EMBL-EBI site) calculating similarity scores to be between 86 and 94%. At the resolutions attained using negative staining and single particle analysis methods, the three-dimensional volume reported here for $Ca_V3.1$ can used to represent $Ca_V1.2$ and thus should provide some insights as to how the cardiac LTCC is formed by several other subunits associating with $Ca_V1.2$. Similarly, this type of modeling could inform upon how $Ca_V3.1$ might bind auxiliary proteins, as although no auxiliary subunits have been identified, as discussed above, there is evidence to suggest that $\alpha_2\delta$-1, when co-expressed with T-type channels, results in enhancement of the calcium channel currents. To carry out this analysis, we have calculated a new three-dimensional structure for a monomeric form of the cardiac LTCC.

Purification of Cardiac LTCCs—Previously, we have reported the isolation of dimeric forms of the skeletal and cardiac muscle LTCCs (22). We have now prepared LTCC monomers by the introduction of two additional steps to the purification procedure: (i) a detergent exchange step replacing digitonin with decyl-β-D-maltoside (1% w/v) during the first chromatographic step and (ii) size-exclusion chromatography. Presented in Fig. 4*A* is an SDS-PAGE (silver-stained) of the purified LTCC showing four main bands at ~240 kDa (α1), 130 kDa (α2), β (~60 kDa), and δ (~30 kDa). The silver-stained band corresponding to the α2 subunit is very faint; however, Western blotting with a monoclonal anti-α2 antibody (Abcam) confirmed the presence and identity of this polypeptide with a molecular mass of ~130 kDa

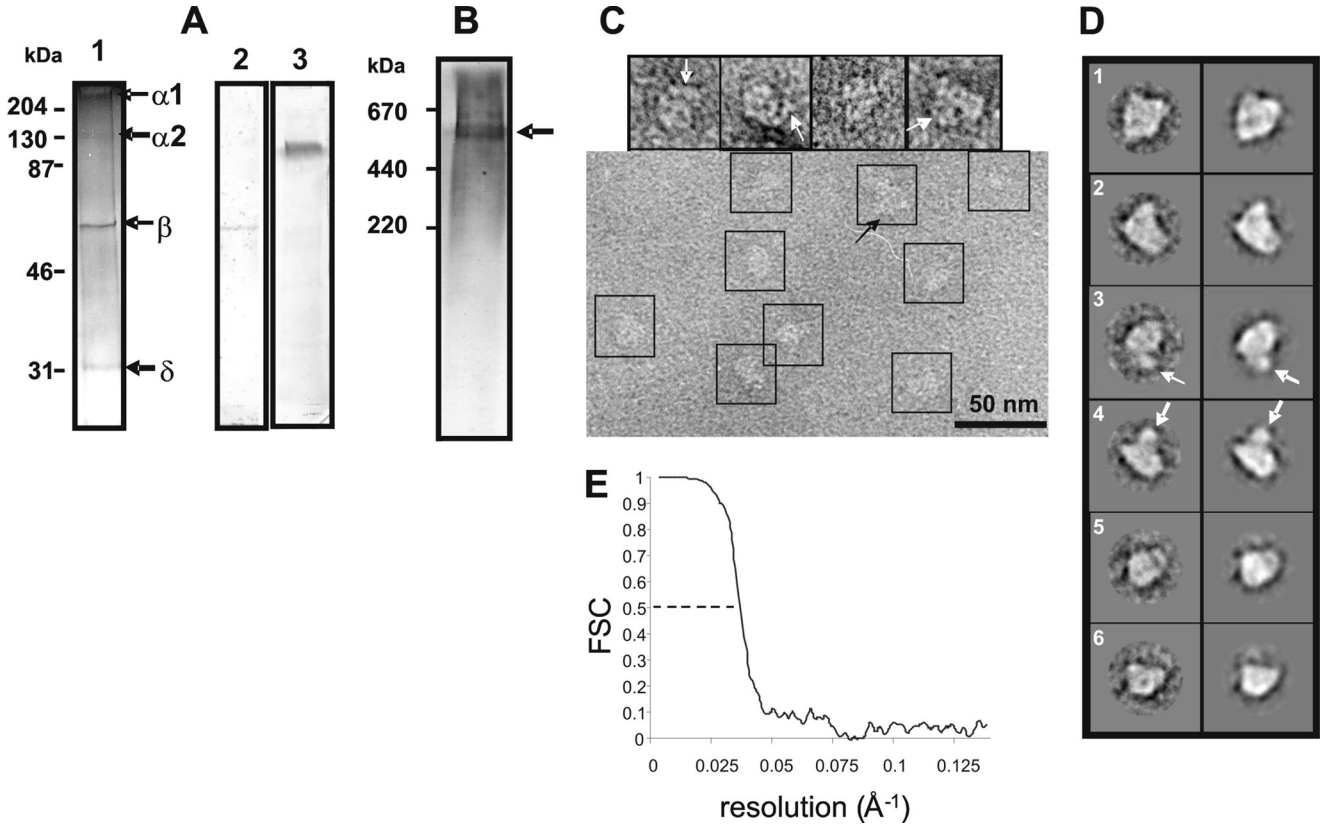

FIGURE 4. **Purification and image analysis of cardiac LTCCs.** *A*, silver-stained SDS-PAGE of purified cardiac LTCC revealing a composition of four protein bands (*lane 1*) with molecular masses of ~240, 130, 55, and 30 kDa corresponding to $Ca_V1.2$ ($\alpha1$), $\alpha2$-, β-, and δ-polypeptides. *Lane 2*, Western blot with anti-β-serum (23), and *lane 3*, anti-$\alpha2$ (Abcam). *B*, silver-stained native gel of the purified LTCC with the principal protein band at ~540 kDa. *C*, field of negatively stained (2% w/v uranyl acetate) purified cardiac LTCC revealing a population of particles presenting a range of orientations ~100–170 Å in size, as indicated in the *boxes*. In one of the images, the complex can be seen to be roughly ellipsoidal with a protruding density indicated by an *arrow*. Examples of raw particles of the cardiac LTCCs are shown above (box size: 302 × 302 Å). *D*, class averages (*left-hand column*) and corresponding reprojections of the final three-dimensional cardiac LTCC volume (*right-hand column*) illustrating a good correlation (box size: 302 × 302 Å). The class average in *panel 1* shows an almost heart-shaped complex with a height of ~160 Å that is ~125 Å wide at the top narrowing toward the base. A small protuberant domain is observed in class averages in *panels 3* and *4*, as indicated by the arrows. Class averages in *panels 5* and *6* show views of the complex ~125 and 100 Å in diameter. Several of the class averages also appear to have a central region of low density. The corresponding back projections of the final three-dimensional volume are presented in the adjacent column, illustrating good agreement between the two. *E*, Fourier shell correlation plot indicating at a correlation of 0.5 that the cardiac three-dimensional LTCC structure is at a resolution of 25 Å.

(Fig. 4*A*, *lane 3*). Silver staining is not a quantitative method, with the intensity of the band being dependent upon a number of physicochemical properties of the protein. In particular, glycosylated proteins often do not stain well, *e.g.* Ref. 38. Gel electrophoresis under non-denaturing conditions revealed that the purified protein has a molecular mass of ~540 kDa (Fig. 4*B*), in contrast to our previous preparations of both the cardiac and the skeletal LTCCs describing dimers of mass >800 kDa (22, 23). As discussed above, the association of detergent micelles to integral proteins upon solubilization from the native membrane leads to an increased protein mass, and thus ~540 kDa can be equated to a monomeric cardiac LTCC with a predicted molecular mass of ~450 kDa with additional detergent and residual lipid bound. The molecular mass of the skeletal muscle LTCC monomer was also reported to be ~550 kDa (39). Although the skeletal muscle LTCC has an additional γ subunit (~30 kDa), $Ca_V1.2$ is believed to be larger than $Ca_V1.1$ by about 30 kDa, and thus it would be predicted that the molecular masses for both complexes would be roughly similar.

Three-dimensional Structure of the Cardiac LTCC Monomer—Shown in Fig. 4*C* is a sample area of a micrograph of negatively stained purified cardiac LTCCs showing particles ranging from ~130 to 170 Å in size. Above the sample micrograph area are some examples of the raw particles presenting different views of the LTCC. A good sampling of multiple views of the LTCC complex was found, permitting implementation of the Fourier common lines projection matching method, using the EMAN software package (27), to determine the LTCC complex three-dimensional structure. Examples of class averages presenting different views of the complex are shown in Fig. 4*D* with the plot in Fig. 4*E* showing that the resolution, estimated by the FSC method, for the final LTCC monomer three-dimensional structure is at ~25 Å.

The three-dimensional volume of the cardiac LTCC monomer (Fig. 5, *A*–*F*) shows a structure comprised of two distinct portions, a heart-shaped body with a density we have termed the "finger" domain extending out from the body, in keeping with the structural features we identified in studies of the dimer form of the LTCC. The body is ~170 Å in height with a width and depth of ~140 and 120 Å, respectively, being wider at the top, tapering toward the base (Fig. 5, *A* and *B*). The finger can be seen to protrude from a density at the tip of the body domain we

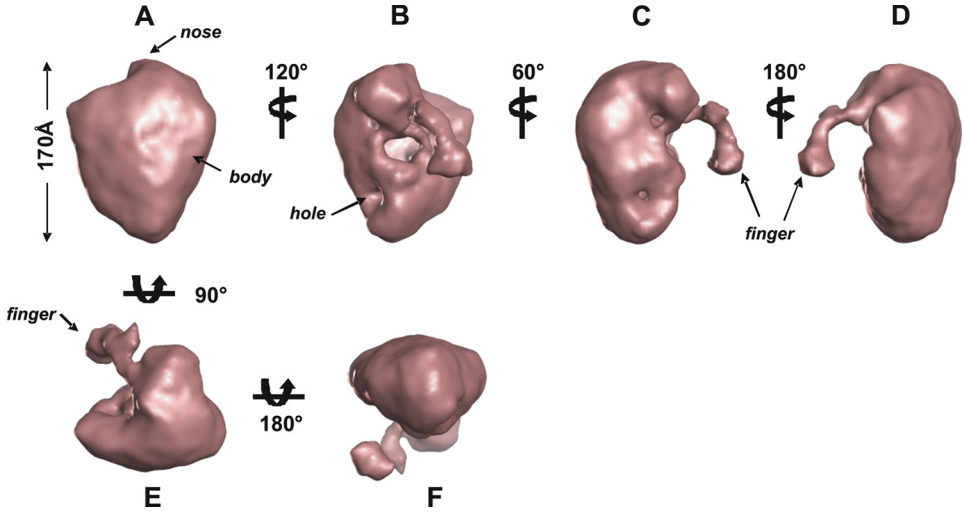

FIGURE 5. **Three-dimensional structure of the monomeric cardiac LTCC displayed at a threshold to encompass a protein mass of ~540 kDa.** *A*, the putative side view (*i.e.* perpendicular to the membrane plane) of the cardiac LTCC monomer shows a complex ~170 Å tall and ~135 Å across at the widest point tapering toward the base. *B–D*, rotation of the view in *A* around the *y* axis counterclockwise reveals that the finger domain is ~90 Å in length and has a hook-shaped formation comprised of several interconnecting domains. The orientation shown in *B* reveals that the structure, behind the finger domain, is open to the extracellular milieu through a series of gaps in the outer surface. A small perforation in the outer surface (labeled *hole*) that forms a tunnel leading into the center of the structure can be seen in *B* and *C*. *E*, rotation of the view presented in *panel A* around the *x* axis 90° away from the plane of the page reveals the top of the structure with a density we have termed the finger domain extending out from the body. *F* shows the base of the complex.

have termed the "nose," a feature we also identified in the cardiac LTCC dimer volume (22). Further details of the finger segment can be seen in Fig. 5, *C–E*, showing that it extends away from the body by ~25 Å and is folded into a "hook" conformation.

Comparison of the Cardiac LTCC Monomer with the Skeletal Muscle Form—The structure for the cardiac LTCC described here allows for a direct comparison with the skeletal muscle LTCC calculated from cryo-EM images (39) emd-1069.map (available through the EmDep Deposition Tool). As shown in Fig. 6*A*, there is a good match in terms of overall size between the two LTCCs (cardiac displayed in *pink mesh* and skeletal portrayed in *green solid surface*). In particular, the length of the cardiac finger density maps well onto the "leg" domain of the skeletal muscle LTCC, with the angle of protrusion and extension away from the main body of the complex also matching. Furthermore, it can be seen that the width of the two structures is similar, except that the skeletal muscle volume is more rounded when compared with the cardiac LTCC, which is tapered toward the base of the volume; this may be due to the absence of the γ subunit in the cardiac LTCC assembly. Matching this new structure with the cardiac dimer volume (22) is less straightforward because association of two monomers will have led to some conformational changes.

Labeling and Orientation of the Cardiac LTCC Monomer within the Sarcolemmal Membrane—Following the strategy described in Ref. 28, we employed concanavalin A (ConA) to label the extracellular portion of the cardiac LTCC complex. ConA at pH 7 is known to form an asymmetric tetramer (40); analysis of the ConA sample by negative staining found a homogeneous population of particles ranging from 3 to 6 nm in size (data not shown). In this form, ConA has exposed carbohydrate binding sites that can associate with the *N*-linked oligosaccharide moieties of the $\alpha_2\delta$ subunit of the cardiac LTCC. Examination of samples of tetrameric ConA with purified cardiac LTCC by transmission electron microscopy after negative staining allowed selection of LTCC-ConA complexes, and using reference-free alignment and classification algorithms, a series of class averages was generated, examples of which are presented in Fig. 6*B*. Class averages in *panels 1* and *2* show views of the LTCC with the finger domain (indicated by the *white arrow*) extending out to the right of the body with a further density (Con A) bound (indicated by the *black arrow*) to the finger. Examination of the three-dimensional structure suggests that these views represent partial face-on orientations of the complex with the ConA associating with a portion of the finger density. Class averages in *panels 3* and *4* show the putative side view of the LTCC complex (~170 Å tall), with the ConA attached to the wider end of the body in a manner that looks distinct from the labeling of the finger domain. Because the α2 and δ polypeptides are both highly glycosylated, the identification of two possible binding sites is reasonable. These data support our previous interpretation of the cardiac LTCC dimer three-dimensional volume with the finger domain and tip of the complex representing the extracellular portion of the cardiac LTCC corresponding to the α2 and δ polypeptides.

Employing our novel structure for $Ca_V3.1$ reported here, we have modeled this volume to represent $Ca_V1.2$ in the new cardiac LTCC monomer map. Fig. 7, *A* and *B*, show putative side views of the cardiac LTCC (*pink mesh*) with the $Ca_V3.1$ volume (*turquoise solid iso-surface*) and crystal structures for $K_V1.2$ (PDB entry 2A79) (*magenta helices*) and β-core (PDB entry 1T3L) (*blue helices*, AID domain in *red*) accommodated within the complex volume. As would be predicted, there is some overhanging $Ca_V3.1$ density in the region assigned to the cytoplasmic domain, but this agrees with the differences in the predicted topology of the two channel proteins (Fig. 1*A*). Fig. 7*C* shows an orientation of the cardiac LTCC to illustrate a perforation in the outer surface of the structure that leads to an inner chamber. $Ca_V3.1$ is not shown on this figure for clarity, but it can be seen from Fig. 2 that the cytoplasmic domains are punctuated by a number of orifices that, when modeled as shown here, line up with the side hole in the LTCC complex.

The structures shown in Fig. 7 also provide new information as to how both the $\alpha_2\delta$-subunit and the β-subunit may associate with $Ca_V1.2$. Subtraction of the $Ca_V3.1$ map from the LTCC three-dimensional structure leaves a volume that correlates to a protein mass of ~210 kDa, which equates to the combined mass of the β- and $\alpha_2\delta$-polypeptides (taking into account that

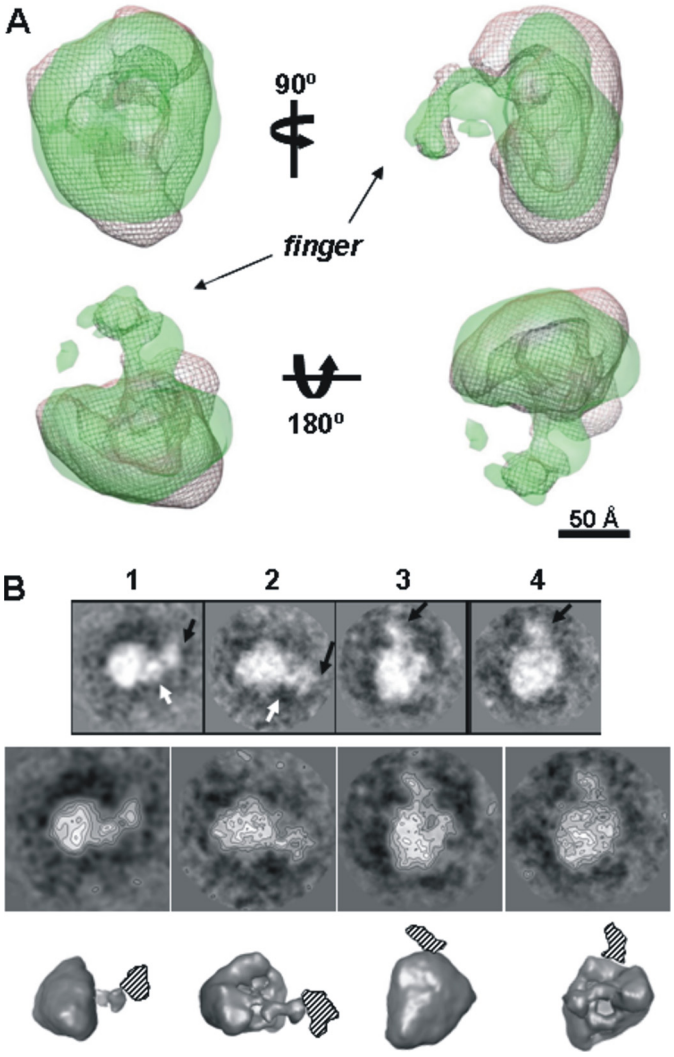

FIGURE 6. **Comparison of the three-dimensional structure of the cardiac LTCC monomer and the monomeric skeletal muscle LTCC and labeling of the glycosylated moieties of the purified cardiac LTCC.** *A*, matching of the cardiac LTCC monomer (*pink mesh*) with the three-dimensional volume reported by Wolf *et al.* (39) (*green iso-surface*), illustrating that both structures have a similar overall height and width with a good correlation between the size, conformation, and orientation of the finger domain of the cardiac LTCC described here and the leg density of the skeletal muscle LTCC. *B*, examples of LTCC class averages, each containing between 30 and 65 LTCC complexes labeled with ConA. At pH 7, ConA forms a stable asymmetric tetramer (3–6 nm in size) binding to *N*-linked glycosylation sites. Selected particles were subjected to alignment and classification methods with four of the principal class averages presented. Class averages in *panels 1* and *2* show putative face-on views of the complex with a ConA tetramer associated with the finger domain. The averaged images in *panels 3* and *4* are side views of the complex with ConA bound toward the tip of the complex. Box size = 374 × 374 Å. The *white arrows* indicate the "finger domain," and the *black arrows* indicate the additional ConA density attached.

$Ca_V3.1$ is ~20 kDa larger than $Ca_V1.2$). We propose, in agreement with labeling studies, that the region above the $Ca_V3.1$ volume extending up to the nose and around to the finger domain corresponds to $\alpha_2\delta$ (Fig. 7, *D–G*, $\alpha_2\delta$ shown in *green*). This orientation places the intracellular β-subunit toward the narrow end of the LTCC complex partially fitting into the pocket formed by the cytoplasmic domains of $Ca_V3.1$. For clarity, similar views of the LTCC are shown in *panels D* and *E* with only the $K_V1.2$ crystal structure shown.

DISCUSSION

The data presented here show the first views of a T-type voltage-gated calcium channel polypeptide, at low/medium resolution. The placement of the $K_V1.2$ crystal as shown in Fig. 3 is consistent with the lower domain (termed C) being formed by the cytoplasmic segments and in agreement with experiments identifying the C-terminal domain, by virtue of its His tag. As shown in Fig. 1*A*, $Ca_V3.1$ has two large cytoplasmic domains forming loops between IS6 and IIS1 (~38 kDa, amino acids 396–743) and IIS6 and IIIS1 (~31 kDa, amino acids 965–1272) with a smaller loop of ~7 kDa between IIIS6 and IVS1 (amino acids 1538–1610). The three-dimensional volume of $Ca_V3.1$ shows that the C domain is indeed formed by several large densities extending below the region assigned to the lipid bilayer to form a vestibule that is in many respects reminiscent of the organization of the intracellular domains of the voltage-sensitive sodium channel (34). Furthermore, the organization proposed here shows that the pore of the $K_V1.2$ channel lies directly above the chamber formed by the putative cytoplasmic domains (Fig. 4*B*), thus providing a passageway for calcium ions to exit through into the cytosol. Intracellular loops of Ca^{2+}, K^+, and Na^+ channels have been suggested to form domains that act as a "ball and chain" or "hinged lid" that play central roles in channel gating as well as binding sites for β auxiliary subunits. Current data suggest that the T-type channel inactivation process probably also operates by involving multiple domains, *i.e.* the S6 helix in repeats I and II (41, 42), the selectivity filter (43), and the C terminus (44). A recent report has also determined that the proximal region (first 55 amino acids) of the I-II loop functions as a gating particle with the distal portion effecting trafficking to the plasma membrane (45). Although the I-II and II-III cytoplasmic loops are not completely resolved from each other in the three-dimensional volume presented here, they can be seen to form ridges of protein density (*e.g.* Fig. 2*B*). This arrangement of the intracellular domains forms an exposed surface that is accessible for forming structural associations with regulatory proteins to exert cellular effects. For example protein kinase C has been described to stimulate $Ca_V3.1$ with effects localized to the II-III loop (46).

We have also reported a three-dimensional structure for a monomeric cardiac LTCC, in contrast to the channel dimers described previously (22). The isolation of a monomeric cardiac, LTCC, cannot be solely attributed to the detergent exchange step because purification of the skeletal muscle channel monomers also employed digitonin (39) but probably relates to the number of purification steps, the endogenous lipids co-purified, and channel complex stability. Our experiences suggest that lipid association plays a role, and we have previously described how dilution with buffer not containing lipids coupled with a further size exclusion chromatography step led to a partial dissociation of the cardiac dimers to monomers (22). It may be, therefore, that the introduction of the detergent exchange step has tipped the monomer-dimer balance in the subsequent purification steps we employed, resulting in less co-purifying lipid and thus favoring the monomer form.

We noted that both the finger of the cardiac LTCC and the tail domain of $Ca_V3.1$ have similar characteristics in that they

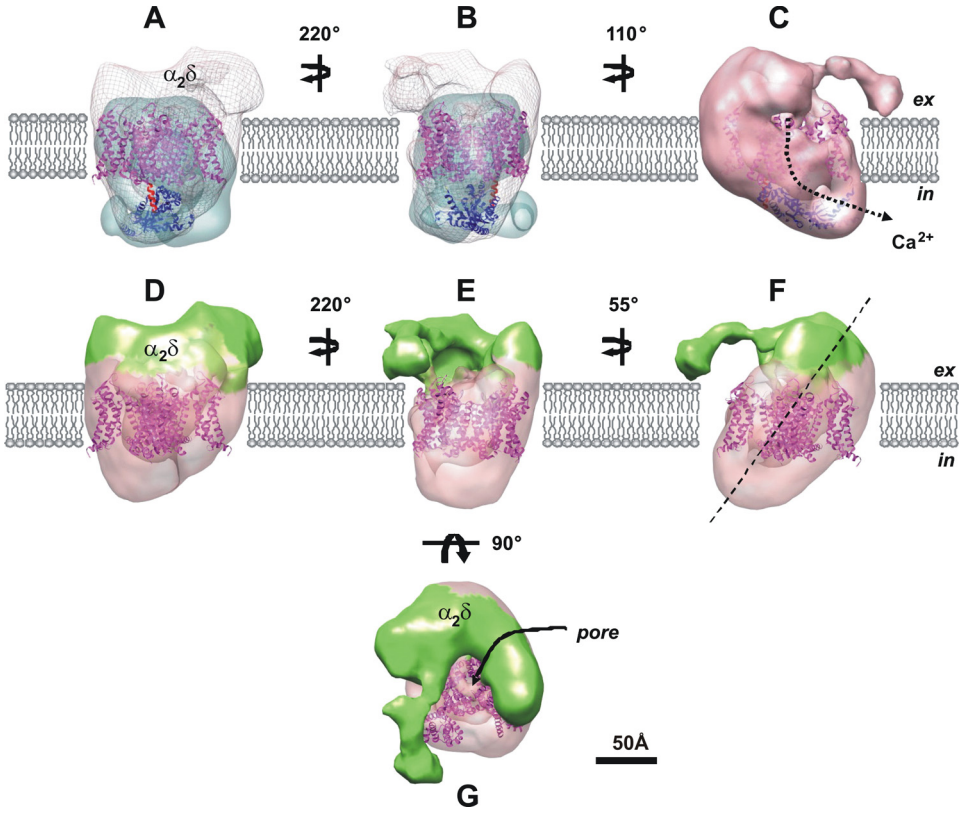

FIGURE 7. **Cardiac LTCC three-dimensional structure, orientation and fitting of $Ca_v3.1$.** *A* and *B*, LTCC three-dimensional volume (*pink mesh*) with the three-dimensional volume of $Ca_V3.1$ (surface-rendered in *turquoise*; transparency setting 0.7) with the TM domains represented by the crystal structure of $K_V1.2$ (PDB entry 2A79) (TM domain, *magenta ribbon*) and the β-core (*blue ribbon*) crystal structure in complex with the $Ca_V1.2$ AID peptide (PDB entry 1T3L) (*red helix*) fitted in the putative cytoplasmic domains. The $Ca_V3.1$ volume matched to the lower portion of the LTCC three-dimensional structure, with the crystal structure of the transmembrane domain of $K_V1.2$ (analogous to the TM region of both LVA and HVA channels) indicating the putative position of the lipid bilayer. The crystal structure of the β-core fits into a pocket formed by the cytoplasmic domains of $Ca_V3.1$ and the narrow end of the LTCC volume. *C*, LTCC three-dimensional structure surface-rendered in *pink*, with structures fitted as in *A* and *B* but with $Ca_V3.1$ not shown to indicate the position of a side hole in the outer surface of the LTCC volume, which also corresponds to a region of low density (a perforation in the $Ca_V3.1$ volume) with the structures organized as shown here. The *dashed line* indicates a possible route of Ca^{2+} translocating across the plasma membrane. *ex*, extracellular; *in*, intracellular. *D* and *E*, Similar views to those shown in *A* and *B*, respectively, but with only the putative position of the lipid bilayer shown by the TM domain of $K_V1.2$, permitting an outline of the extracellular $\alpha2$ subunit to be visualized (colored *green*). The $Ca_V3.1$ volume and β-core crystal structure are still modeled within the LTCC but not shown (using the Model panel in Chimera). *F*, side view of the cardiac LTCC illustrating how the complex has been orientated by tilting the long axis of the complex ~50° with respect to the plane of the lipid bilayer. *G*, top view of the complex revealing further details of the organization of the $\alpha2$ polypeptide forming a cap over the top of the Ca_V subunit but with the ion channel pore open to the extracellular milieu.

extend out from the main protein density. However, a comparison of the two finds that the tail is much shorter than the finger segment with a different orientation and angle of extension from $Ca_V3.1$ when compared with the way in which the finger domain protrudes out from the body of the cardiac LTCC. Moreover, modeling of the two structures so that the finger domain corresponds to the C terminus of $Ca_V1.2$ found that the majority of the protein density would lie within the membrane, which is not consistent with known topology, and consequently, it would seem that this is not the case. Furthermore, modeling of the two structures as shown in Fig. 7 shows that the region attributed to the C-terminal domain of $Ca_V1.2$ will be intimately associated with the β-polypeptide and thus is likely not resolved in the cardiac LTCC three-dimensional volume.

Murata *et al.* (47) first reported two-dimensional projection images of negatively stained (uranyl acetate) monomeric rabbit skeletal muscle LTCCs, describing a rod-like structure with a height of ~210 Å and diameter of ~100 Å with a small spherical domain extending from the upper portion of the rod. Labeling studies led to the proposal that the skeletal muscle channel spans the T-tubular membrane by ~210 Å with the spherical density corresponding to the $\alpha2$ polypeptide placed on the extracellular side. This work was followed by the first three-dimensional structure of a skeletal muscle LTCC monomer by Serysheva *et al.* (48) determined from frozen hydrated protein. However, the three-dimensional volume was found to be substantially smaller (~115 × 130 × 120 Å), but the proposed orientation of the two principal domains, termed a heart and a handle region, agreed with that of Murata *et al.* (47), with an asymmetric distribution of protein density across the bilayer, consistent with the predicted topology. The three-dimensional monomer structure for the skeletal muscle LTCC described by Wolf *et al.* (39) a year later was not only larger than the other directly comparable structure from Serysheva *et al.* (48) but was positioned so that the majority of the protein density was within the membrane, leaving only the leg domain extending into the extracellular milieu. On the basis of labeling of the intracellular and extracellular polypeptides of the channel dimers studied by this group, we proposed a similar orientation of the skeletal and cardiac dimer structures, with respect to the lipid bilayer, as that suggested by the Murata (47) and Serysheva (48) groups and in contrast to that proposed by Wolf *et al.* (39).

We have now advanced this work further and show a direct comparison between the monomeric cardiac LTCC structure described here and the skeletal muscle LTCC structure of Wolf *et al.* (39), finding them to be very similar. Our new structure shows that the finger extends out from the nose density that lies directly above the domain ascribed to the $Ca_V1.2$ ion channel pore subunit, and so, in agreement with our ConA labeling, we suggest that this region is also attributable to a portion of the $\alpha_2\delta$ protein. As shown in Fig. 7, fitting of the $Ca_V3.1$, $K_V1.2$, and β-core crystal structures into the LTCC three-dimensional volume also allows the approximate region corresponding to $\alpha_2\delta$ to be defined (Fig. 7, *C–F*) (due to the small size of the δ polypeptide, we cannot resolve it from α_2). This region corre-

sponds to a protein mass of ~170 kDa (at the thresholds displayed here) and has been colored *green* to give an impression of the shape, size, and architecture of the $\alpha_2\delta$ polypeptide. The $\alpha_2\delta$ subunit forms a "cap" on the top of the Ca_V polypeptide, and the view shown in Fig. 7*G* reveals that the pore of $Ca_V1.2$ is open to the extracellular milieu below the $\alpha_2\delta$. This arrangement suggests that several extracellular domains of $Ca_V1.2$ are likely to be engaged in binding $\alpha_2\delta$. We have previously noted that both the LTCC α2-subunit and many cell adhesion molecules, including integrin β-subunit, contain a Von Willebrand factor-A domain with a metal ion-dependent adhesion site motif and that integrin dimers form a loose hairpin structure (15). It is therefore interesting to find that the details of the finger domain shown here reveal that it also forms a hook-shaped structure.

The new structure for $Ca_V3.1$ described here also allows us to propose another orientation for the LTCC complex, whereby the long axis traverses the plasma membrane as shown in Fig. 7*F*, tilted at an angle of ~50° with respect to the plane of the bilayer. An alternative orientation would be whereby the long axis is orthogonal rather than tilted; however, this would place a portion of the finger domain (which corresponds to the $\alpha_2\delta$ polypeptide) within the lipid bilayer. Because this domain may be quite flexible in its native environment *in vivo*, there may be movement of the finger placing it above the membrane, and so this orientation cannot be discounted. An alternative interpretation would be one in which the finger domain corresponds, in part, to the transmembrane δ, but because only a single helix is suggested to span the membrane, then the volume of the finger domain (even accounting for associating detergent) is much too large. Therefore, on the basis of the data we currently have available, we propose the orientation as shown in Fig. 7, *C* and *F*.

The model in Fig. 7 places the HVA β-subunit nestled between the base of the $Ca_V3.1$ with the C terminus wrapped around and the AID domain in close proximity to the TM assembly. This arrangement helps explain how the β-polypeptide may bind to $Ca_V1.2$ because in addition to the interaction domain crystallized with the β-subunit (AID), there are multiple reports of other interaction sites between β and α1, which would be consistent with the β-subunit fitting, in part, into the pocket formed by the cytoplasmic domains of $Ca_V3.1$. For example, the N terminus (49), regions between loops I-II (50) and III-IV (51), and the C terminus (52) of various α1 polypeptides have all been implicated in interactions with the β-subunit. The β-polypeptide as shown here is exposed to the cytoplasm from the base of the structure and thus is also able to bind regulatory proteins (53). This arrangement leads to a region of low density identified in the surface-rendered LTCC volume, Fig. 5, *B* and *C*, labeled *hole*, and thus it is tempting to suggest that this organization of polypeptides forms a tunnel leading to the interior of the structure and may be the exit route for Ca^{2+} from the LTCC into the cytosol after translocation across the lipid bilayer passing through the ion channel as illustrated in Fig. 7*C*.

Our study presents the first three-dimensional structure of a T-type voltage-gated calcium channel. T-type channels are critical components of a multitude of fundamental physiological processes. However, the mechanisms underlying LVA channel regulation and control are still largely unknown, and thus the structure presented here, and details resolved, represent an important step forward to closing the gaps in current knowledge and pave the way for future structure-function studies.

Acknowledgment—We thank Leon Douglas for help in protein expression.

REFERENCES

1. Tsien, R. W., Ellinor, P. T., and Horne, W. A. (1991) *Trends Pharmacol. Sci.* **12,** 349–354
2. Zhang, J. F., Ellinor, P. T., Aldrich, R. W., and Tsien, R. W. (1994) *Nature* **372,** 97–100
3. Hofmann, F., Lacinová, L., and Klugbauer, N. (1999) *Rev. Physiol. Biochem. Pharmacol.* **139,** 33–87
4. Huguenard, J. R. (1996) *Annu. Rev. Physiol.* **58,** 329–348
5. Perez-Reyes, E. (2003) *Physiol. Rev.* **83,** 117–161
6. Vassort, G., and Alvarez, J. (1994) *J. Cardiovasc. Electrophysiol.* **5,** 376–393
7. Yunker, A. M., and McEnery, M. W. (2003) *J. Bioenerg. Biomembr.* **35,** 533–575
8. Ertel, E. A., Campbell, K. P., Harpold, M. M., Hofmann, F., Mori, Y., Perez-Reyes, E., Schwartz, A., Snutch, T. P., Tanabe, T., Birnbaumer, L., Tsien, R. W., and Catterall, W. A. (2000) *Neuron* **25,** 533–535
9. Leung, A. T., Imagawa, T., and Campbell, K. P. (1987) *J. Biol. Chem.* **262,** 7943–7946
10. Arikkath, J., and Campbell, K. P. (2003) *Curr. Opin. Neurobiol.* **13,** 298–307
11. Van Petegem, F., Chatelain, F. C., and Minor, D. L., Jr. (2005) *Nat. Struct. Mol. Biol.* **12,** 1108–1115
12. Opatowsky, Y., Chen, C. C., Campbell, K. P., and Hirsch, J. A. (2004) *Neuron* **42,** 387–399
13. De Jongh, K. S., Warner, C., and Catterall, W. A. (1990) *J. Biol. Chem.* **265,** 14738–14741
14. Ellis, S. B., Williams, M. E., Ways, N. R., Brenner, R., Sharp, A. H., Leung, A. T., Campbell, K. P., McKenna, E., Koch, W. J., Hui, A., Schwartz, A., and Harpold, M. M. (1988) *Science* **241,** 1661–1664
15. Cantí, C., Nieto-Rostro, M., Foucault, I., Heblich, F., Wratten, J., Richards, M. W., Hendrich, J., Douglas, L., Page, K. M., Davies, A., and Dolphin, A. C. (2005) *Proc. Natl. Acad. Sci. U.S.A.* **102,** 11230–11235
16. Jay, S. D., Sharp, A. H., Kahl, S. D., Vedvick, T. S., Harpold, M. M., and Campbell, K. P. (1991) *J. Biol. Chem.* **266,** 3287–3293
17. Letts, V. A., Felix, R., Biddlecome, G. H., Arikkath, J., Mahaffey, C. L., Valenzuela, A., Bartlett, F. S., 2nd, Mori, Y., Campbell, K. P., and Frankel, W. N. (1998) *Nat. Genet.* **19,** 340–347
18. Dubel, S. J., Altier, C., Chaumont, S., Lory, P., Bourinet, E., and Nargeot, J. (2004) *J. Biol. Chem.* **279,** 29263–29269
19. Perez-Reyes, E., Cribbs, L. L., Daud, A., Lacerda, A. E., Barclay, J., Williamson, M. P., Fox, M., Rees, M., and Lee, J. H. (1998) *Nature* **391,** 896–900
20. Page, K. M., Heblich, F., Davies, A., Butcher, A. J., Leroy, J., Bertaso, F., Pratt, W. S., and Dolphin, A. C. (2004) *J. Neurosci.* **24,** 5400–5409
21. Jones, L. R. (1988) *Methods Enzymol.* **157,** 85–91
22. Wang, M. C., Collins, R. F., Ford, R. C., Berrow, N. S., Dolphin, A. C., and Kitmitto, A. (2004) *J. Biol. Chem.* **279,** 7159–7168
23. Wang, M. C., Velarde, G., Ford, R. C., Berrow, N. S., Dolphin, A. C., and Kitmitto, A. (2002) *J. Mol. Biol.* **323,** 85–98
24. Berrow, N. S., Campbell, V., Fitzgerald, E. M., Brickley, K., and Dolphin, A. C. (1995) *J. Physiol.* **482,** 481–491
25. Adair, B., Nunn, R., Lewis, S., Dukes, I., Philipson, L., and Yeager, M. (2008) *Biophys. J.* **94,** 2106–2114
26. Böttcher, B., Wynne, S. A., and Crowther, R. A. (1997) *Nature* **386,** 88–91
27. Ludtke, S. J., Baldwin, P. R., and Chiu, W. (1999) *J. Struct. Biol.* **128,** 82–97
28. Lazarov, V. K., Fraering, P. C., Ye, W., Wolfe, M. S., Selkoe, D. J., and Li, H. (2006) *Proc. Natl. Acad. Sci. U.S.A.* **103,** 6889–6894
29. Frank, J., Radermacher, M., Penczek, P., Zhu, J., Li, Y., Ladjadj, M., and Leith, A. (1996) *J. Struct. Biol.* **116,** 190–199

30. Ruprecht, J., and Nield, J. (2001) *Prog. Biophys. Mol. Biol.* **75,** 121–164
31. Zhang, X., Settembre, E., Xu, C., Dormitzer, P. R., Bellamy, R., Harrison, S. C., and Grigorieff, N. (2008) *Proc. Natl. Acad. Sci. U.S.A.* **105,** 1867–1872
32. Rosenberg, M. F., Callaghan, R., Ford, R. C., and Higgins, C. F. (1997) *J. Biol. Chem.* **272,** 10685–10694
33. Okorokov, A. L., Orlova, E. V., Kingsbury, S. R., Bagneris, C., Gohlke, U., Williams, G. H., and Stoeber, K. (2004) *Nat. Struct. Mol. Biol.* **11,** 1021–1022
34. Sato, C., Ueno, Y., Asai, K., Takahashi, K., Sato, M., Engel, A., and Fujiyoshi, Y. (2001) *Nature* **409,** 1047–1051
35. Gennis, R. B. (1989) in *Biomembranes, Molecular Structure and Function* (Cantor, C. R., ed) pp. 91–105, Springer-Verlag, New York
36. Quillin, M. L., and Matthews, B. W. (2000) *Acta Crystallogr. D Biol. Crystallogr.* **56,** 791–794
37. Larkin, M. A., Blackshields, G., Brown, N. P., Chenna, R., McGettigan, P. A., McWilliam, H., Valentin, F., Wallace, I. M., Wilm, A., Lopez, R., Thompson, J. D., Gibson, T. J., and Higgins, D. G. (2007) *Bioinformatics* **23,** 2947–2948
38. Gradilone, S. A., Arranz, S. E., and Cabada, M. O. (1998) *Anal. Biochem.* **261,** 224–227
39. Wolf, M., Eberhart, A., Glossmann, H., Striessnig, J., and Grigorieff, N. (2003) *J. Mol. Biol.* **332,** 171–182
40. Bouckaert, J., Hamelryck, T., Wyns, L., and Loris, R. (1999) *Curr. Opin. Struct. Biol.* **9,** 572–577
41. Arias, J. M., Murbartián, J., Vitko, I., Lee, J. H., and Perez-Reyes, E. (2005) *FEBS Lett.* **579,** 3907–3912
42. Marksteiner, R., Schurr, P., Berjukow, S., Margreiter, E., Perez-Reyes, E., and Hering, S. (2001) *J. Physiol.* **537,** 27–34
43. Talavera, K., Janssens, A., Klugbauer, N., Droogmans, G., and Nilius, B. (2003) *J. Gen. Physiol.* **121,** 529–540
44. Staes, M., Talavera, K., Klugbauer, N., Prenen, J., Lacinova, L., Droogmans, G., Hofmann, F., and Nilius, B. (2001) *J. Physiol.* **530,** 35–45
45. Baumgart, J. P., Vitko, I., Bidaud, I., Kondratskyi, A., Lory, P., and Perez-Reyes, E. (2008) *PLoS ONE* **3,** e2976
46. Park, J. Y., Kang, H. W., Moon, H. J., Huh, S. U., Jeong, S. W., Soldatov, N. M., and Lee, J. H. (2006) *J. Physiol.* **577,** 513–523
47. Murata, K., Odahara, N., Kuniyasu, A., Sato, Y., Nakayama, H., and Nagayama, K. (2001) *Biochem. Biophys. Res. Commun.* **282,** 284–291
48. Serysheva, I. I., Ludtke, S. J., Baker, M. R., Chiu, W., and Hamilton, S. L. (2002) *Proc. Natl. Acad. Sci. U.S.A.* **99,** 10370–10375
49. Stephens, G. J., Page, K. M., Bogdanov, Y., and Dolphin, A. C. (2000) *J. Physiol.* **525,** 377–390
50. Herlitze, S., Hockerman, G. H., Scheuer, T., and Catterall, W. A. (1997) *Proc. Natl. Acad. Sci. U.S.A.* **94,** 1512–1516
51. Geib, S., Sandoz, G., Cornet, V., Mabrouk, K., Fund-Saunier, O., Bichet, D., Villaz, M., Hoshi, T., Sabatier, J. M., and De Waard, M. (2002) *J. Biol. Chem.* **277,** 10003–10013
52. Gerhardstein, B. L., Puri, T. S., Chien, A. J., and Hosey, M. M. (1999) *Biochemistry* **38,** 10361–10370
53. Dolphin, A. C. (2003) *Pharmacol. Rev.* **55,** 607–627